METAL SEMICONDUCTOR METAL PHOTODETECTORS

The two-terminal device discussed here converts optical power into an electric current. This basic photodetector, which is mainly based on an interdigitated electrode structure, benefits from a simple fabrication process. It can offer a large photosensitive surface area and leads to high speed performance. This article describes the basic physical mechanisms of this device, the material used in its fabrication and technology, and its main performance.

The metal–semiconductor–metal (MSM) photodetector is one of the solid-state photodetectors fabricated on semiconductor slices. The general principle of photodetection in semiconductor material is to collect electron-hole pairs that have been generated by light absorption. The main condition for

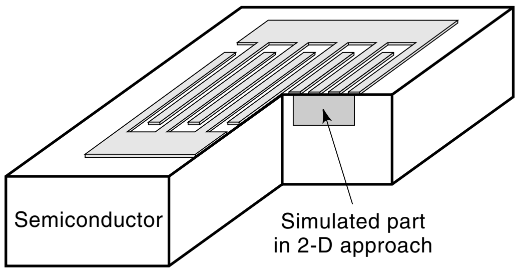

Figure 1. Typical structure of metal–semiconductor–metal photodiode.

this absorption is

$$h\nu \geq E_g$$

where ν is the optical wave frequency, h the Planck constant, and E_g the semiconductor energy bandgap. Once photogenerated, the carriers move to the photodetector electrodes by diffusion or conduction. The PIN, Avalanche, and MSM photodiodes use a depleted zone where a high electric field separates photocarriers and drives them as quickly as possible to the electrodes. The MSM photodiode consists of two metallic Schottky contacts deposited on a low-doped absorbing semiconductor material. Usually, the structure is planar and the two contacts take the form of interdigitated fingers, as presented in Figure 1 (it can be top, back, or side illuminated). This type of design allows for a large photosensitive surface area, while keeping a short distance between the fingers. Indeed, this type of photodetector is generally intended to work under very short light pulses (some picoseconds or even smaller) or with high-frequency–modulated light signals (up to several tens of gigahertz). Moreover, the number of technological steps needed to make such a photodetector is small. In some cases, only the Schottky contact deposition by electron beam evaporation is needed to make the photodetector. These features make this photodetector particularly attractive for monolithic integration with microelectronic devices, for example, amplifiers, to constitute receivers. This device is interesting for a large range of applications, such as high data bit rate fiber-optic receivers in the field of optical telecommunications (short or long distance), optical interconnects, or high-speed optical sampling.

MSM photodetector performance depends on the depleted zone extension, the electric field strength in the different regions of the semiconductor, and the dark current. Moreover, as for all other photodetectors, the different device properties to be considered are responsivity, bandwidth, and noise. We will first consider the essentials to understanding the total behavior of this photodetector. So, we look at the current-voltage characteristic in darkness in relation to the depletion region extension; then we present an overview of the properties due to the planar interdigitated structure, particularly the carrier paths between the electrodes and the electric field distribution. In this way, we examine the carrier transit time distribution inside the photodetector. Then we present an overview of the different fundamental sources of the dark current. This first part concludes with a short paragraph on the optimum bias voltage of the MSM.

The second part of this article is devoted to semiconductor epitaxial structure and device features. After the description of the whole epitaxial structure in the different material systems used to fabricate MSM photodetectors, we analyze their responsivity for various illumination conditions, the unintentional gain observed in this device (like in photoconductors), the different phenomena that limit the bandwidth, the source of the dominant noise, and some scaling rules. For each parameter, experimental results reflect the typical characteristics obtained in each material system.

Finally, we briefly introduce some types of integrated devices in which the MSM photodiode is the key element, that is, electrooptic sampling cells and monolithic integrated receivers.

PRINCIPLES

Metal–Semiconductor–Metal Photodiode Without Illumination Versus Bias Voltage

Let us consider two metallic Schottky contacts on a uniformly low or unintentionally doped n-type semiconductor. The energy-band diagram of this structure at thermodynamic equilibrium, presented in Fig. 2, shows the two depletion regions (width W_1 and W_2, respectively) inherent to the metal-semiconductor junctions. Each depletion region space charge is due to the ionized donor atoms whose electrons now act as surface charge at the metal-semiconductor interfaces. ϕ_{m1} and ϕ_{m2} are the work functions of metal 1 and 2, respectively, χ is the semiconductor electron affinity, and E_f is the Fermi level. The potentials across these two depleted zones are V_{b1} and V_{b2}, built-in potentials of the contacts. This whole structure is equivalent to two Schottky barriers connected back to back. Their barrier height is ϕ_{n1}, ϕ_{n2} for electrons, and ($\phi_{p1} + V_{b1}$), ($\phi_{p2} + V_{b2}$) for holes. We have (1):

$$\phi_{n1,2} = \phi_{m1,2} - \chi \tag{1}$$

and

$$\phi_{p1,2} = E_g - (\phi_{m1,2} - \chi) \tag{2}$$

At thermodynamic equilibrium, the summation of all currents due to carrier transport through barriers is equal to zero. When a voltage is applied, the dark current of the structure

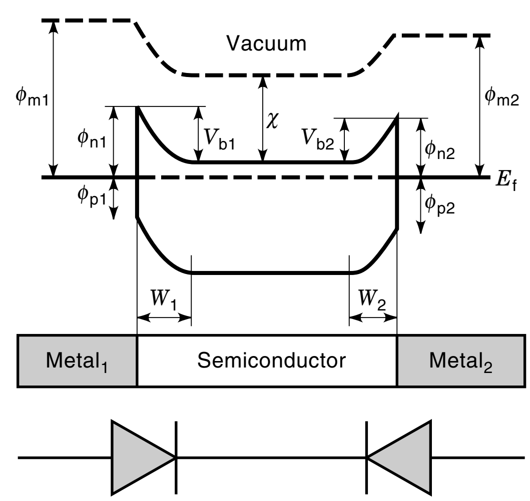

Figure 2. Energy-band diagram of an MSM structure at thermodynamic equilibrium; the semiconductor is n-type, unintentionally or low doped.

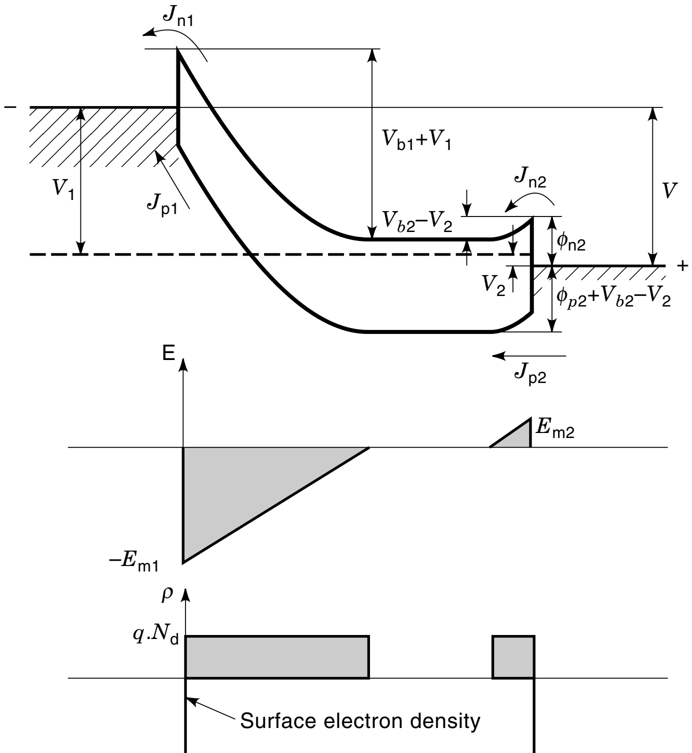

Figure 3. Energy-band diagram of a biased MSM structure with electric field and charge density distributions; the applied voltage is $V = V_1 + V_2$, $V < V_{RT}$.

is due to carriers passing through the metal-semiconductor interfaces. Considering the energy-band diagram of the biased structure presented in Fig. 3, for equal contact surface areas, and neglecting the recombination processes inside the neutral zone between the two depletion regions, we have:

$$J_{n1} = J_{n2} \tag{3}$$

$$J_{p1} = J_{p2} \tag{4}$$

and

$$J_{dark} = J_n + J_p \tag{5}$$

As a consequence, contact 1 is reverse biased (potential V_1) while contact 2 is forward biased (potential V_2), with

$$V = V_1 + V_2 \tag{6}$$

The electron current is limited by the first contact while the hole current is limited by the second. These limitations depend on the transport process through the barriers. Following the analysis presented in Ref. 2, whether this transport process is due to thermionic emission or tunneling effect (assisted or not), there are two noteworthy bias voltages for this structure (Fig. 4).

The read-through voltage V_{RT}, when the semiconductor (width L) is just fully depleted,

$$W_1 + W_2 = L$$

and the flat-band voltage V_{FB} (Fig. 4), corresponding to the relations

$$W_1 = L \text{ and } W_2 = 0$$

Knowing that:

$$W_1 = \sqrt{\frac{2\epsilon_s(V_{b1}+V_1)}{qN_d}} \tag{7}$$

and

$$W_2 = \sqrt{\frac{2\epsilon_s(V_{b2}-V_2)}{qN_d}} \tag{8}$$

where ϵ_s is the semiconductor permittivity and N_d its doping level, we obtain

$$V_{FB} = \frac{qN_dL^2}{2\epsilon_s} - V_{b1} + V_{b2} \tag{9}$$

V_{RT} is close to V_{FB} (2). For bias voltage lower than V_{RT}, the holes injected through contact 2 diffuse in the neutral region between the two depleted zones and some of them recombine. Increasing bias voltage results in a decrease of the neutral region width and so of the recombinations. Consequently, the dark current increases quickly. Above V_{RT}, almost all injected carriers at one electrode are collected at the other. The increase of dark current with bias voltage is slower. It depends on the nature of the transport process through Schottky barriers and on the electric field at each contact. Generally, for $V > V_{FB}$, the electric field increases in the device and particularly near electrode 1 (the cathode). If it is sufficiently high, tunneling or impact ionization probability increases sharply at this place; the breakdown process occurs and the dark current increases very quickly with bias voltage. The typical I-V characteristic of a GaAs MSM photodiode with low dark current is reported in Fig. 5. We will complete this brief analysis by a review of the different transport processes reported in MSM photodiodes. But any analysis of the MSM-I-V characteristic cannot be carried out without considering the specific problems due to its planar structure.

Specific Properties Due to Planar Structure

For a bias voltage higher than the flat-band voltage, the electric field distribution in the semiconductor between two fin-

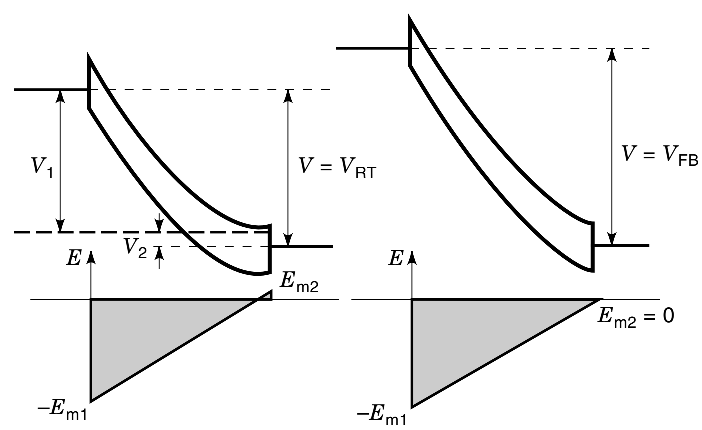

Figure 4. Energy-band diagrams of a biased MSM structure with electric field for applied voltages of V_{RT} and V_{FB}.

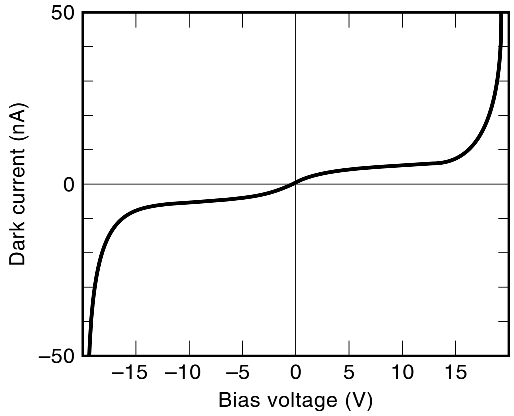

Figure 5. Measured dark current voltage characteristic of a GaAs MSM photodetector.

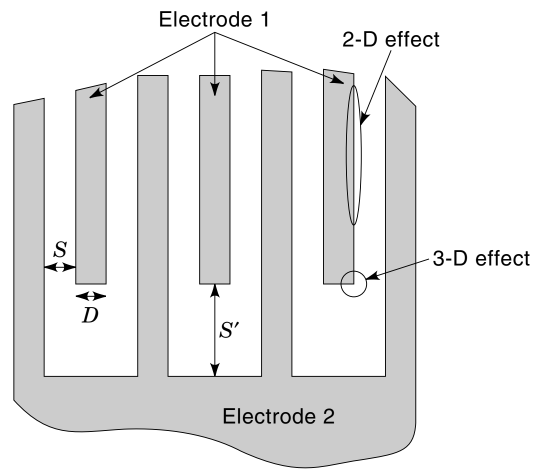

Figure 7. Two-dimensional and 3d corner effects in interdigitated structure. S is the electrode spacing, D the finger width, and S' the electrode distance.

gers, calculated by bidimensional Poisson equation solution, is similar to the one presented in Fig. 6. This calculation is made for a GaAs doping level of 10^{14}cm^{-3}. There are two electric field maxima at the contact edges. This bidimensional effect becomes three dimensional at the tip of each finger (Fig. 7). As a result of this particular electric field distribution, breakdown will occur first

- At the finger tips
- Near the semiconductor surface between two finger edges.

In order to avoid parasitic breakdown located at the finger tips, the common method is to set a distance S' between the two metallic electrodes larger than the electrode spacing S, as shown in Fig. 7. This solution appears clearly in Refs. 3 to 5. It is also possible to round the finger tips, as reported, for example, in Ref. 6, or to design a specific finger form without corners (7). Anyway, the effect due to finger edges cannot be avoided, and the main part of the dark current will flow near the semiconductor surface between two different fingers. The electric field is high (approximately 20 kV/cm in our example) in the vicinity of the semiconductor surface and the deeper we go in the semiconductor, the weaker the electric field is. The field lines (perpendicular to the equipotential lines) of the modeled structure presented in Fig. 8 illustrate the carrier paths between fingers. Obviously, the deeper the carrier's location, the longer the distance it has to cover to join the electrode, and since its velocity is electric field dependent, the longer the time to be collected by the electrode. For example, supposing electron–hole pair photogeneration along the O–y line of Fig. 8, the transit time needed for an electron or hole to join the electrodes is plotted in Fig. 9 versus the depth at which it has been photocreated. The electron and hole field-dependent velocity in GaAs used for this calculation is from (8). Compared to carriers generated near the semiconductor surface, those generated at 2 μm depth have a transit time to electrodes 5 times and 3 times greater for, holes and electrons, respectively.

Analysis of Dark Current

The MSM photodetector dark current has to be as small as possible in order to reduce excess noise in the optoelectronic receiver and, consequently, to lower the minimum detectable

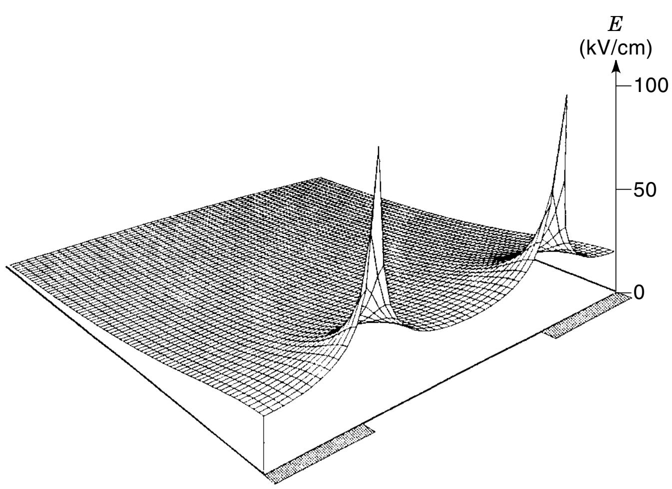

Figure 6. Electric field distribution in a GaAs MSM photodetector between two fingers. In this example, electrode spacing and finger width are 2 μm, absorbing layer is 3.5 μm thick and the bias voltage 8 V.

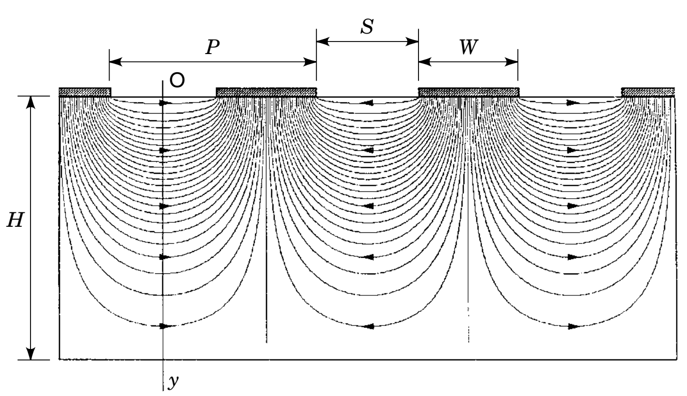

Figure 8. Example of field lines in a GaAs MSM photodetector. The simulated zone is that of Fig. 1. The arrows indicate the direction of electron transport on each line. O–y line is used in the following figure. P is the Period, S the electrode Spacing and D the finger Width.

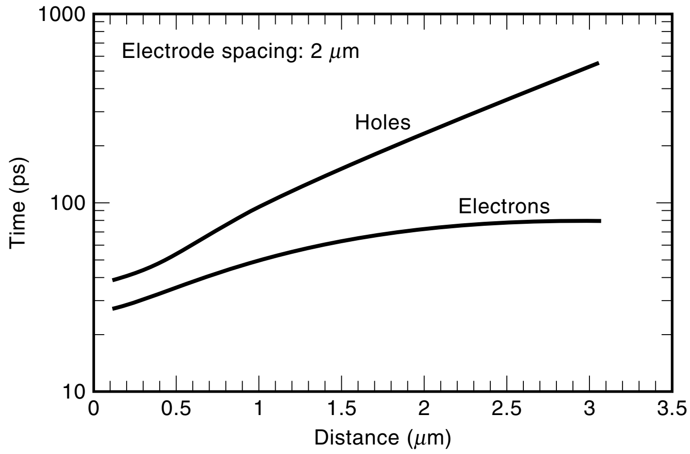

Figure 9. Required transit time for electrons and holes photogenerated at a certain depth on the O–y line of Fig. 8 to join the electrode.

power (9). More generally, this current depends strongly on the shape of the potential barrier at electrodes under bias. The different mechanisms that can occur in these conditions are (1,10):

1. Emission over the Schottky barrier (thermionic emission process)
2. Tunneling and thermionic field emission
3. Thermal generation of carriers in the depleted zone or in the neutral region and, in case of defects inducing states in the forbidden bandgap, mainly:
    1. Carrier generation assisted by states within the forbidden bandgap
    2. Tunneling through the metal–semiconductor barrier assisted by states in the forbidden bandgap

Assuming at first that the material is lattice matched and without defects inducing states in the forbidden bandgap, we are limited to the three first mechanisms. Assuming also that there is no unintentional thin insulating layer between the semiconductor and the electrode and that the material doping level is low, the thermionic emission process dominates over tunneling processes due to the strong dependence of the tunneling probability on doping level; moreover, it dominates over thermal generation processes because the material resistivity is high. This predominant process is the dark current limiting factor. If V_B is the breakdown voltage, for $V_{FB} < V < V_B$, following the analysis of Sze et al. (2), we have:

$$J_{\text{dark}} = \left[A_n^* T^2 \cdot \exp\left[-\frac{q(\phi_{n1} - \Delta\phi_{n1})}{kT}\right] + A_p^* T^2 \cdot \exp\left[-\frac{q(\phi_{p2} - \Delta\phi_{p2})}{kT}\right]\right] \cdot \left[1 - \exp\left(-\frac{qV}{kT}\right)\right] \tag{10}$$

where $A^*_{n,p}$ are the effective Richardson constants for electrons and holes, T is the absolute temperature, and $\Delta\phi_{n1,p2}$ are the barrier lowering values due to the image force effect. This barrier lowering depends on the electric field $E_{m1,2}$ at each contact (1)

$$\Delta\phi_{n1,p2} = \sqrt{\frac{qE_{m1,2}}{4\pi\epsilon_s}} \tag{11}$$

which explains the slow increase of the dark current with bias voltage. The dark current is due to electrons emitted at the cathode (J_{n1}) and to holes emitted at the anode (J_{p2}) (Fig. 3). It depends essentially on the barrier heights at the two contacts. For example, in the case of MSM photodiodes fabricated on a low-doped GaAs layer, if the electrodes 1 and 2 are made of the same metal, we have:

$$\phi_{n1} + \phi_{p2} = E_g = 1.42 \text{ eV} \tag{12}$$

So, a Schottky barrier lower than $E_g/2 = 0.71$ eV makes the electron current predominant by increasing the probability of electron transport over the barrier of the contact 1, while a barrier higher than 0.71 eV makes the hole current predominant by increasing the hole emission at the contact 2. As a result, as shown by Wada & al and as presented in Fig. 10, the tungsten Silicide WSi_x is the most suitable contact to decrease the GaAs MSM photodiode dark current because its barrier height is near 0.71 eV. Such a study has been confirmed by Koscielniak et al. (11). By the same way of analysis, an interesting solution to decrease the dark current consists in the deposition of an electrode metal with a high electron barrier at the cathode and another one, with a high hole barrier, at the anode. Such an approach has been successfully applied by Wohlmuth et al. in the case of InGaAs/AlInAs MSM photodiodes with Pt/Ti/Pt/Au and Ti/Au for the cathode and anode metalizations, respectively. The dark current of this assymetric structure was 0.2 nA at 5 V (10).

These results demonstrate the existence of a dominant thermionic process, but the other mechanisms can become dominant, depending on the perturbation of the metal-semiconductor interface during the technological process. All phenomena leading to hole accumulation in the vicinity of the

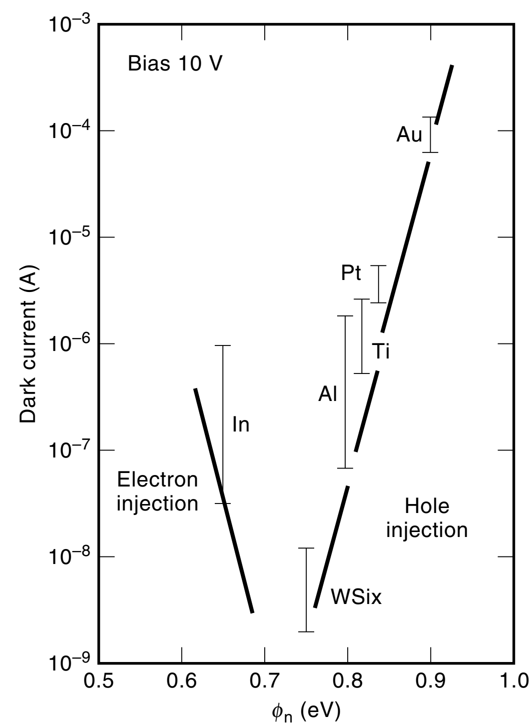

Figure 10. Dark current versus metal-semiconductor energy barrier for a biased GaAs MSM structure. This curve is reprinted from Wada et al. (Ref. 6) with permission of *IEEE Journal of Quantum Electronics.*

cathode, or electron accumulation near the anode, will modify the energy band structure at the interfaces and increase the tunneling probability at these electrodes. Within this context, electron tunneling assisted by hole accumulation in a thin native insulating layer between metal and semiconductor (GaAs) has been reported by Sugeta et al. (12), and hole tunneling due to electron accumulation in a hollow conduction band in the bidimensional potential distribution has been suggested by Wada et al. (6).

Tunneling assisted by deep levels inside the forbidden bandgap has also been reported by Wehmann et al. (13) in the specific case of heteroepitaxy of InGaAs on silicon.

Finally, a review of the dark current problems must mention the gain phenomena (see section on gain). Moreover, like most micro- and optoelectronic devices, an MSM photodetector has to be carefully passivated. Usually, the thickness of the dielectric layer used (SiO_2 or Si_3N_4) is chosen to act also as an antireflection coating (6,14). This insulating layer can be deposited

1. Above the fingers and the pads
2. Above the fingers and under the pads
3. Under the fingers and the pads

The two last solutions need comment. The dielectric insulating layer under pads as well as fingers is used as a barrier enhancement layer, to decrease the dark current (15), and to avoid photocurrent gain due to surface states (see section on gain). But in most cases, the barrier enhancement layer is a large bandgap lattice matched or mismatched semiconductor epilayer. Insulating only under the pads leads to a decrease of the dark current (16,17) and also to a decrease of the photodetector parasitic capacitance (18). This solution has been adopted mainly when the photodiode is integrated in a coplanar microwave line (9).

Optimum Bias Conditions of MSM Photodetector

From the above descriptions, we can conclude that the electric field has to be sufficiently high to allow the quick collection of photogenerated carriers. Because of the specific bidimensional distribution, this requires a high bias voltage, particularly for large interelectrode spacing. Moreover, because the dark current has to be kept as low as possible, we must avoid breakdown conditions. This leads to

$$V_{\mathrm{FB}} < V < V_{\mathrm{B}}$$

But an optimum bias voltage can be difficult to find since the electric field distribution is not homogeneous and the edge effect can lead to breakdown while the electric field is still small in the electrode gap. The larger the interelectrode spacing, the higher the difference between the electric field in the gap and those at finger edge. This makes the small interelectrode spacing interesting.

EPITAXIAL STRUCTURE AND DEVICE PROPERTIES

Material Systems

Obviously, the MSM photodetector epitaxial structure is designed starting from the absorbing layer whose gap is small enough to absorb at the wavelength of operation. The successive structure evolutions have led to the whole epitaxial structure presented in Fig. 11. This structure is the most that can be encountered; usually all epilayers are not required or used.

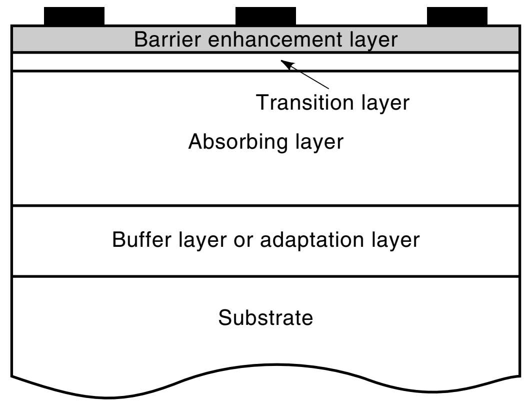

Figure 11. Whole MSM photodetector epitaxial structure.

The different absorbing materials already used are presented in the Table 1 with the corresponding enhancement barrier and transition epilayers. If the Schottky barrier obtained by direct metal deposition on the absorbing epilayer is sufficiently high to induce low dark current (some tens of nanoamperes at 5 or 10 V bias voltage), the MSM photodetector structure is reduced to its simplest form (i.e., two Schottky contacts on an absorbing layer). This is, for example, the case in GaAs MSM photodetectors, as already explained in the previous section. But in the (1.0 to 1.6 μm) wavelength domain, the Schottky barrier obtained on N-$Ga_{0.53}In_{0.47}As$ is low, near 0.2 eV (40), which compels introduction of a large-gap enhancement-barrier layer. This layer has been grown in lattice-mismatched GaAs, AlGaAs, InP-GaInP, or in lattice-matched Fe:InP, P+ GaInAs, $Al_{0.48}In_{0.52}As$. Its thickness is a few hundred angstroms. The enhancement-barrier epilayer has also been introduced on GaAs (often in lattice-matched AlGaAs) in order to reduce the dark current and to improve the photodetector reliability (32). Furthermore, in the case of the GaAs-based photodiode, a large-gap bottom insulating layer can be used to limit the absorbing layer thickness and, consequently, to decrease the transit time of photogenerated carriers (Fig. 9). In the case of silicon, this insulating layer is silicon dioxide and the photodetector is then directly fabricated on commercially available SIMOX (separation by implanted oxygen) wafer (35,37). It is also possible to use sapphire substrate (34). The heterointerface between the absorbing layer and the enhancement-barrier layer leads to electron and hole pile-up with recombinations, a phenomenon which decreases the responsivity as well as the bandwidth. This is why a transition layer, a compositionally graded layer or a graded superlattice, is sometimes added. The impact of this layer on the photodetector dynamic behavior will be considered later. In order to demonstrate the state of the art, we sum up in Table 2 some typical realizations with their metallization and dark current. This table demonstrates the possibility obtaining dark current of a few nanoamperes or even less than 1 nA in each wavelength domain for an MSM photodetector active area, allowing the absorption of the whole light beam issued from a fiber. The active area is indi-

Table 1. MSM Photodetector Epitaxial Structure (The Heteroepitaxial Structures on Silicon Substrate Are Not in This Table)

Wavelength	Absorbing Material	Substrate	Enhancement-barrier Layer	Transition Layer
Ultraviolet $\lambda < 0.3\ \mu$m	GaN	Saphire	—	
	SiC	SiC	-(33)	
$\lambda < 1.1\ \mu$m	Si	Si	-(34–37)	
$\lambda < 0.87\ \mu$m	GaAs	GaAs	-(6, 9)	
			AlGaAs (4, 18, 19, 20)	—
			GaInP (21)	—
Long wavelength	$Ga_{0.53}In_{0.47}As$	InP	$Al_{0.48}In_{0.52}As$ (22, 23)	In(GaAl)As graded (16, 23, 28)
$1.0\ \mu m < \lambda < 1.6\ \mu m$				AlInAs-GaInAs GSL (28, 29)
			P+ $Ga_{0.53}In_{0.47}As$ (31)	
			Fe:InP (7)	
			GaAs * (24)	
			InP-GaInP * (25)	
			AlGaAs * (26)	
Far infrared	HgCdTe	GaAs*	CdTe (27)	
$\lambda > 1.3\ \mu$m	GaSb	GaSb	AlGaSb (30)	

*Lattice mismatched GSL: graded superlattice

cated even if we have to keep in mind that the dark current is correlated with the contact area value. In most commonly reported designs, this later value is close to the half of the active area value. MSM photodiodes with transparent electrodes have been included. We did not introduce the GaInAs-based devices heteroepitaxially grown on Si or on GaAs substrate. By using these growth techniques, high responsivity (1.0 to 1.6 μm) wavelength photodetectors whose fabrication is compatible with GaAs or Si founderies were obtained (43,44).

Illumination Conditions and Responsivity

The photodetector can be top-, back-, or side-illuminated through an integrated optical waveguide. For top-illuminated structures, the light has to propagate through the interelectrode region into the semiconductor. Neglecting the recombinations, the quantum efficiency is then given by

$$\eta = (1 - R) \cdot \frac{S}{(S + D)} \cdot [1 - \exp(-\alpha \cdot W_a)] \tag{13}$$

where R is the reflection coefficient of light at the air-semiconductor interface. R is reduced to a few percent in case of the use of an antireflection coating. The ratio $S/(S + D)$ introduces the finger shadowing effect, which is the main drawback of top-illuminated interdigitated structures. The absorption coefficient is α and the absorbing layer thickness is W_a. The responsivity is given by

$$\Re = \frac{q}{h\nu} \cdot \eta \tag{14}$$

where q is the electron charge (absolute value), and $h\nu$ the photon energy of the incident light. These expressions show

Table 2. Typical MSM Photodetector Material Structures With the Metallization and the Corresponding Dark Current

Ref.	Wavelength Domain	Epitaxial Structure	Growth	Metallization	Active Surface (μm^2)	Dark Current
(35)	<0.9 μm	crist.-Si/SiO_2/Si (SIMOX wafer)	—	Ti-Au	5 × 5	0.05nA (1V)
(38)	<0.9 μm	crist.-Si/amorph.-Si-H	(PECVD)	Cr-Au	100 × 100	0.4 nA(10V)
(6)	<0.85 μm	GaAs(S.I.)/GaAs	VPE	Wsi_x	100 × 100	1nA (10V)
(18)	<0.85 μm	GaAs(S.I.)/GaAs/AlGaAs	MOCVD	Ti-Pt-Au	75 × 75	0.04nA (10V)
(32)	<0.85 μm	GaAs(S.I.)/GaAs/AlGaAs/GaAs/ AlGaAs/GaAs	MOCVD	Ti-Pt-Au	20 × 50	0.3nA (10V)
(22)	1.3–1.55 μm	InP(S.I.)/GaInAs/AlInAs	LPMOCVD	Ti-Au	50 × 50	20nA (10V)
(41)	1.3–1.55 μm	InP(S.I.)/InP/GaInAs/InP	GSMBE	Pt-Au	50 × 50	200nA (10V)
(43)	1.3–1.55 μm	InP(Fe)/GaInAs(Fe)/InP(Fe)	LPMOCVD	Ti-Au	100 × 100	200nA (10V)
(25)	1.3–1.55 μm	InP(Fe)/InP/GaInAs/InP/GaInP	LPMOCVD	Au**	100 × 100	30nA (10V)
(23)	1.3–1.55 μm	InP(S.I.)/AlInAs/GSL/GaInAs/ GSL/AlInAs	GSMBE	Ti-Pt-Au	30 × 30	5nA (10V)
(16)	1.3–1.55 μm	InP(S.I.)/AlInAs/GaInAs/ In(GaAl)As/AlInAs	MBE	Ti-Au	50 × 50	109nA (10V)
(42)	1.3–1.55 μm	InP(Fe)/AlInAs/GaInAs/ In(GaAl)As/AlInAs	MOVPE	ITO **	50 × 50	4nA (5V)
(27)	>1.5 μm	GaAs*/HgCdTe/CdTe	MOCVD	Pt-Au	48 × 40	70 nA (5V)
(33)	0.33–0.39 μm	6H-SiC/SiC	—	Cr-Au	100 × 100	1nA (80V)

*Lattice mismatched; **Transparent fingers; GSL: graded superlattice; S.I.: semi-insulating that the MSM photodetector responsivity strongly depends on the absorbing layer thickness, the material absorption coefficient, and the interdigitated structure.

In the long wavelength region, GaInAs absorbing coefficient is 1.16 μm^{-1} at 1.3 μm and 0.68 μm^{-1} at 1.55 μm wavelength (45). The absorbing coefficient of GaAs is 1 μm^{-1} around 0.8 μm wavelength and it is lower than 0.2 μm^{-1} for $\lambda > 0.7$ μm (close to 0.2 μm^{-1} at 0.8 μm) and higher than 1 μm^{-1} for $\lambda < 0.5$ μm (34) for crystalline silicon. All these material properties mean a penetration length close to 1 μm for III–V materials. Because of indirect bandgap transition, the silicon penetration length is higher than 10 μm near 0.8 μm wavelength and lower than 1 μm only for $\lambda < 0.5$ μm. The calculated external quantum efficiency and responsivity of MSM photodetectors with different absorbing materials is presented in Table 3. Two absorbing layer thicknesses of 1 μm and 1000 Å have been used for calculation allowing to appreciate the photodetector sensitivity in typical cases. For these calculations, we supposed a perfect antireflection coating ($R = 0$) and equal finger width and spacing ($S = D$).

As for the finger shadowing effect, it seems that the finger width must be decreased as far as possible, but the finger resistance then increases, which reduces the photodetector bandwidth (Fig. 16). The finger resistance depends obviously on the finger dimensions, but, as noted by Chou et al. (5) in the case of fingers made of 150 Å/350 Å thick Ti/Au deposited on SiO_2 substrate, the finger resistance per unit length is higher than the one calculated using bulk resistivities. This difference may be due to the electron scattering with the metallic boundaries. Indeed, for fingers wider than 0.1 μm, only the top and bottom boundaries induce an increase of the resistance, while for fingers narrower than 0.1 μm, the side boundaries produce an effect. For example, the measured resistance for 0.06 μm finger width is 80 $\Omega/\mu m$ (11 $\Omega/\mu m$ with bulk resistivity) while it is 4.3 $\Omega/\mu m$ for 0.5 μm (1.2$\Omega/\mu m$ with bulk resistivity) (5). All these results permit us to estimate finger resistance in a great number of cases.

All these reasons generally lead to a finger width not far from the interelectrode spacing ($D \geq S \geq D/4$). However, a way to avoid the finger shadowing effect consists of the use of transparent metallizations in indium tin oxide (ITO), cadmium tin oxide (CTO), tungsten or gold. High–carried-concentration ITO is used with success in the short wavelength domain ($\lambda < 0.85$ μm) where its optical transmittance is greater than 87% (46) and its resistivity is poor. Its transmittance around 1.3 μm and 1.5 μm wavelength is respectively near 70% and 50%, but at 1.3 μm, it increases strongly while decreasing carrier concentration. Nevertheless, a good tradeoff between transmittance and resistivity can be obtained by improving the technological deposition process (42), it is then possible to get a 99.5% transmittance, with a resistivity which is only an order of magnitude higher (0.015 $\Omega \cdot$ cm at room temperature). In the same way, the CTO has a transmittance over 85% in the long wavelength domain, and minimum resistivity can be obtained under specific deposition conditions (46). However, we must keep in mind that sputtering often produces defects at the metal-semiconductor interface, which increase the leakage current (47) and also induce photocurrent gain (this is documented in references 42 and 46). For all these reasons, Chu et al. (47) proposed to deposit on an AlInAs enhancement-barrier layer a thin tungsten silicide (WSi_x : 200 Å) layer under the ITO (550 Å); this dual layer structure allows a 57% optical transmittance at 1.55 μm wavelength. Avoiding sputtering, Matin et al. (21) deposited 300 Å thick tungsten fingers by electron beam evaporation on an InGaP cap layer and obtained a 95% GaAs photodetector quantum efficiency. Yuang et al. (25) improved, the responsivity of a GaInAs photodetector from 0.4 to 0.7 A/W, with an InGaP enhancement barrier layer by depositing 100 Å thick gold fingers. To sum up, the use of transparent fingers allows the improvement of the responsivity, but the holes photogenerated under the anode (and the electrons photogenerated under the cathode) take a very long time to join the other electrode (see Fig. 8); this reduces the photodetector bandwidth by increasing the average transit time of the photogenerated carriers. As a consequence, in case of top illumination, transparent metallization is generally used when the high-speed operation of the device is not of prime importance.

On the other hand, Eq. (13) is acceptable for a period ($P = S + D$) larger than the wavelength. In case of smaller finger period, the electrodes constitute a metallic grating through which light propagation must be studied. This complicated problem, already suggested by Sano (48), has been experimentally studied by Kuta et al. (49). The transmission coefficient through an interdigitated structure depends on:

- The ratios λ/P and S/D
- The optical polarisation: electric field of the optical wave parallel ($\|$) or perpendicular ($\perp$) to the fingers
- The finger thickness
- The semiconductor refraction index n_s

For $S \approx D$, the dominant factor is the ratio λ/P with two particular values: $\lambda/P = 1$ and $\lambda/P = n_s$, where the transmission coefficient reaches a minimum (49). Moreover, the transmission coefficient is higher for perpendicular polarisation than for a parallel one. For $\lambda/P > 1.5$, the external quantum effi-

Table 3. Calculated Quantum Efficiency (η) and Responsivity ($\Re$) of MSM Photodetectors with Different Absorbing Materials for Absorption Layer Thicknesses of 1 μm and 1000 Å. We Supposed $R = 0$ and $S = W$.

		$W_a = 1$ μm			
Wavelength	Material	η	$\Re$ (A/W)	η	$\Re$ (A/W)
0.8 μm	GaAs	31.5%	0.195	4.7%	0.03
1.3 μm	GaInAs	34.3%	0.343	5.5%	0.055
1.55 μm	GaInAs	24.7%	0.29	3.3%	0.04
0.8 μm	crist.-Si	4.7%	0.029	0.5%	0.003
0.6 μm	crist.-Si	16.5%	0.076	2%	0.012
0.4 μm	crist.-Si	50%	0.154	31.6%	0.097

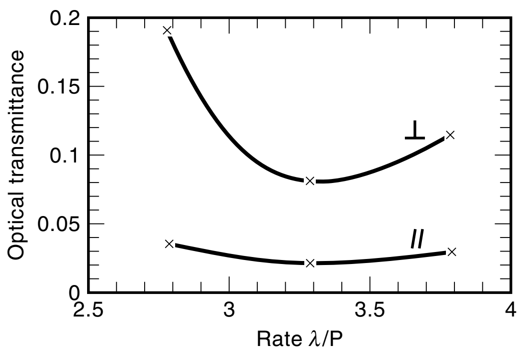

Figure 12. Measured transmittance of a GaAs MSM photodiode with $P = 4000$ Å and $D/P = 0.57$ versus the rate λ/P for linearly polarised light oriented parallel (‖;) or perpendicular (⊥) to the fingers. The lines are guides to the eye. Reprinted with permission from J. J. Kuta et al., Polarization and wavelength dependence of Metal-semiconductor-metal photodetector response, *Appl. Phys. Lett.* **64** (2):140–472, 1994. Copyright 1994 American Institute of Physics.

ciency of linearly parallel polarized light is lower than a few percents. A typical behaviour, presented in Fig. 12, shows the measured optical transmittance of such a grating on GaAs material ($P = 4000$ Å, $D/P = 0.57$) versus λ/P for wavelength higher than 0.85 μm. The interdigitated structure in 550 Å thick Ti–Au has been patterned using electron beam lithography. Because the GaAs is then transparent, the grating influence appears, this means a very low efficiency obtained for parallel linearly polarized light, while a higher one is measured for perpendicular polarization. A minimum exists at $\lambda/P = n_s = 3.4$ because of a resonance effect with the substrate. The studies that can be carried out with modeling tools such as finite difference time domain beam propagation method (FDTD-BPM) also show the great influence of the finger thickness because it is close to the finger width in these conditions. We cannot here describe all the consequences of this complicated problem but we must point out that the modification of photodetector responsivity due to small finger period is sufficiently high to allow the fabrication of a wavelength discriminator using several MSM photodiodes with different periods. Chen et al. (50) did this using two simultaneously illuminated parallel photodetectors with periods of 4000 Å and 6000 Å, respectively ($S = D$). Under these conditions, the photocurrent ratio (I_{4000}/I_{6000}) depends strongly on the wavelength, while it remains unchanged when the optical power varies.

Because of the photodetector planar structure and its specific transit characteristic (Figs. 8 & 9), top-illuminated high-speed devices need a thin absorption layer, which is not compatible with high quantum efficiency. In order to overcome this trade-off, a back reflector can be introduced. Instead of being placed on the back side of the wafer, it is positioned on the bottom of the absorption layer. In the case of III–V materials, this is of a Bragg reflector, while in case of silicon in the 0.8 μm wavelength region, it can be made from metal and needs wafer bonding technique (51). In order to increase the quantum efficiency, another method is roughening the front or back surface of the absorbing layer (37,52), but controlling the absorbing layer thickness is difficult, especially when this thickness has to be of a few thousand angstroms.

Let us consider now the back and side illumination. For back illumination, the substrate must be made thin and polished in order to deposit an antireflection layer. Obviously, the shadowing effect disappears; moreover, the finger presence increases the quantum efficiency by reflecting the light into the absorbing region. Nevertheless, compared to top illumination, the photodetector speed is reduced because of two different phenomena. First, because the generation rate decreases exponentially starting from the absorbing layer bottom, the greater part of the electron-hole pairs is photogenerated near the absorbing layer bottom, which increases the average transit time. Second, as already explained, the carriers photogenerated just under the electrodes have a long transit time. All these considerations explain that back-illuminated MSM photodiodes with very high responsivity (0.96 A/W at 1.3 μm wavelength) have already been made (see, eg., Ref 28) with an MSM photodetector directly integrated with the optical fiber, and also that this illumination condition is chosen if the high speed is not of prime importance.

Finally, the side illumination through an optical waveguide is interesting because it allows decreasing the absorbing layer thickness while absorbing nearly 100% of the light that propagates inside the waveguide (53). However, because a high coupling efficiency between the fiber and the waveguide is difficult to achieve, the responsivity of the whole structure constituted by the photodetector with its waveguide is generally not high. In spite of this problem, the waveguide MSM photodetector is a good candidate in the field of integrated photonic circuits (53,54).

Gain and Recombinations

Among the different electrical mechanisms that influence MSM photodetector responsivity, the recombinations tend to decrease responsivity, whereas trapping effects increase it. The recombinations occur in bulk material, particularly in cases of high impurity or high defect density. Such material as amorphous silicon, Cr-doped GaAs, low-temperature GaAs, Fe-doped InP, or Fe-doped GaInAs holds a short recombination time, which can be used to improve the photodetector dynamic behavior, as will be seen in the next section. But if the recombination time is shorter than the average interelectrode transit time, only a part of the photocarriers will be collected. Anyway, the recombinations abate the responsivity in all cases if the light penetration depth exceeds the depleted zone thickness; the carriers photogenerated outside the depletion region slowly diffuse and some of them recombine. This situation is encountered particularly in crystalline silicon MSM photodetectors in the (0.6 μm to 0.9 μm) wavelength domain, where the absorption coefficient is small. In this case, the quantum efficiency is only a few percent and increases with bias voltage because the depletion region depth increases with bias.

Recombinations also occur at the heterointerfaces, that induce carrier pileup. This is notably often the case between the small-gap absorbing layer and the large-gap Schottky enhancement layer. In this situation, the recombination rate at the heterointerface increases with carrier density and decreases with the electric field, which allows the carriers to surmount the barrier. An example of such behavior, already reported by Yang et al. (55), is given by Burroughes et al.

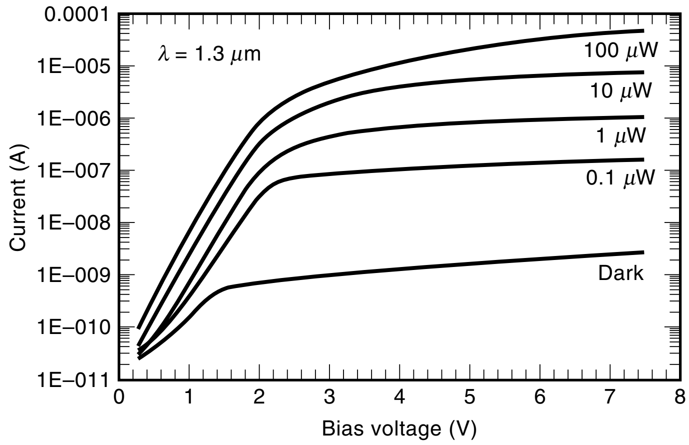

Figure 13. Dark and photocurrent of a top-illuminated InP/GaInAs/AlInAs MSM photodetector versus dc bias voltage. The GaInAs-AlInAs interface is abrupt and with a low defect density. The finger spacing is 3 μm and there is no AR-coating © 1991 IEEE. This curve is reprinted from Ref. 56 with permission.

(56) in Fig. 13 where, for a bias voltage higher than 2 V, the responsivity of a Fe:InP/GaInAs/AlInAs MSM photodiode depends on the optical power as well as on the dc bias voltage. Such a mechanism incites to introduce a transition layer in order to avoid the carrier pile-up; in this case, the abrupt interface with low defect density makes the photodetector compatible with a GaInAs/AlInAs H-MESFET process (56). Moreover, these curves show a responsivity of 0.7 A/W at 7 V bias, which corresponds, according to the authors, with an external quantum efficiency of 160%. Therefore, a gain phenomenon is combined with the effect of abrupt heterointerface. The gain often observed at low bias voltage in MSM photodetectors is due to trapping rather than to impact ionization in the high electric field region near the electrode edges. As reported by Klingenstein et al. (57) in the case of GaAs based photodetectors, two mechanisms can occur with different behavior versus frequency. The first has a specific cut-off frequency lower than a few hundred megahertz and can be compared to the low-frequency gain observed in GaAs photoconductors (58). It varies weakly versus temperature and disappears if a large-gap cap layer is grown on the absorbing layer. This is shown in Fig. 14, which compares the photocurrent-voltage characteristic of an (S.I.) GaAs/GaAs/$Al_{0.6}Ga_{0.4}As$ MBE–grown MSM photodetector to one of an (S.I.) GaAs/GaAs. The traps located at the semiconductor surface between the fingers are responsible for this mechanism. The photogenerated carriers trapped at this surface create a dissymmetric electric charge distribution, the electrons being trapped rather near the anode. This charge modifies the potential distribution at the metal-semiconductor contact, which induces additional carrier injection from the electrode. The injection mechanism is tunneling rather than thermionic emission process, because the latter would make the gain strongly temperature dependent, which is not the case. For every trapped hole, an electron is injected, drifts in the semiconductor and is collected, and so on, until the trapped hole is re-emitted. Therefore, this phenomenon is limited by the trap density at the semiconductor surface, which leads to a gain decrease when the optical power and thus the photogenerated carrier density increase. Gain values of some hundreds then can be observed for a frequency below a few hundred megahertz or even lower.

The second gain mechanism existing at higher frequencies is due to hole pile-up or trapping in the vicinity of the cathode. These holes induce electron injection by tunneling from the electrode. Furthermore, gain due to impact ionization in the semiconductor bulk can also be observed when the electric field strength is sufficiently high. This occurs generally at high bias voltage (12).

Usually, the trapping effect of the surface is cancelled by the Schottky enhancement layer (18,57) and the quality of the metal-semiconductor interface. By doing this, it is possible to reduce the trap density strongly and to suppress the formation of a native thin insulating layer, so to avoid the gain phenomena that increase the photodetector pulse response time by adding a long tail to the short pulse due to collected photocarriers.

Dynamic Behavior

As with all photodetectors, the different phenomena leading to the MSM photodiode dynamic behavior are photodetector capacitance and resistance and carrier transit time. The main advantage of the MSM photodetector is its low capacitance C_{PD}, which can be calculated taking into account the planar structure by using conformal mapping technique (59). For two electrodes with width D and spacing S, (the period is $P = S + D$) above a semi-infinite semiconductor with relative permittivity ϵ_r, the capacitance per unit length is

$$C_0 = \epsilon_0 \cdot (1 + \epsilon_r) \cdot \frac{K(k)}{K(k')} \tag{15}$$

with

$$K(k) = \int_0^{\pi/2} \frac{d\phi}{\sqrt{1 - k^2 \sin^2 \phi}} \qquad k = \tan^2\left[\frac{\pi}{4} \cdot \frac{D}{P}\right] \text{ and}$$

$$k' = \sqrt{1 - k^2}$$

and the capacitance of the MSM photodetector active zone is given by

$$C_{PD} = C_0 \cdot \frac{A}{P} \approx C_0 \cdot (N - 1) \cdot L \tag{16}$$

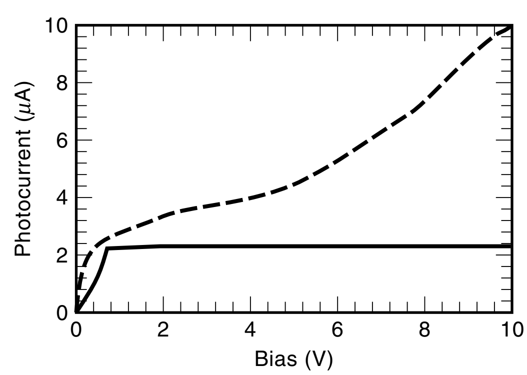

Figure 14. Photocurrent versus bias voltage for two MSM photodetectors with and without cap layer. Dashed line: (SI) GaAs/GaAs-Ti-Pt-Au structure, straight line: (SI) GaAs/GaAs/$Al_{0.6}Ga_{0.4}As$-Ti-Pt-Au structure. These MBE grown photodetectors with 1.5 μm finger spacing are illuminated at 632.8 nm with 20 μW optical power. These experimental results are reprinted from M. Klingenstein et al., Photocurrent gain mechanisms in metal-semiconductor-metal photodetectors, *Solid State Electron,* **37** (2): 333–340. Copyright 1993 with kind permission from Elsevier Science Ltd, The Boulevard, Langford Lane, Kidlington OX5 1GB, UK.

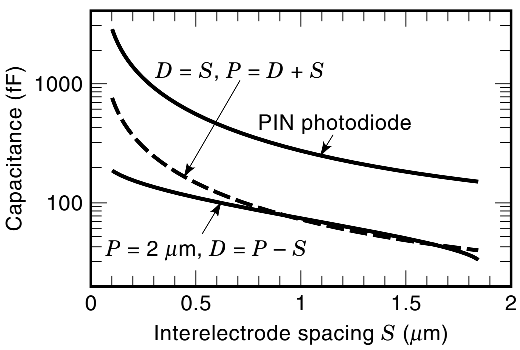

Figure 15. MSM photodetector capacitance versus finger spacing S. The active area is 2500 μm^2. Straight line: constant period so $D = P - S$, dashed line: $D = S$ so $P = D + S$. For comparison, the capacitance of a *pin* photodiode with an active layer thickness equal to S and the same area is plotted.

where A is the photodetector active area, P the period, N the number of fingers, and L the finger length. The comparison of the capacitance of an MSM photodiode with a spacing between 0.2 μm and 2 μm to the capacitance of a *pin* photodiode with an active layer thickness equal to S is shown in Fig. 15. Under these conditions, in spite of their different structures, these two photodetectors have a similar carrier transit time and the same active area—2500 μm^2. As is clear, the MSM photodiode capacitance is more than three times lower than that of the corresponding *pin* photodiode. The third curve of this figure, corresponding to a 2 μm period, shows the decrease of the capacitance when decreasing the finger width while keeping the period constant. This demonstrates the interest in decreasing the finger width compared to the finger spacing, since it also allows enhancement of the responsivity by diminishing the shadowing effect. However, the finger resistance can become important. Such a problem necessitates taking into account the whole MSM photodetector equivalent circuit represented in Fig. 16. I_{PH} represents the photocurrent, R_{PD} the leakage resistance, R_F the finger resistance, C_{PA} the parasitic capacitance including the ground-finger capacitance, that between pads, and the ground-pads capacitance. L_{BW} and C_{BW} are the parasitic elements due to the bond wire and R_L the load. The finger resistance is given by

$$R_F = 2R_0L/N \tag{17}$$

where R_0 is the finger resistance per unit length, L the finger length, and N the number of fingers on each electrode. The typical values of these elements are presented in Table 4.

In most cases, we can neglect the finger resistance and the bond-wire parasitic elements. Thus, only the classical elements R_L and $C_{MSM} = C_{PD} + C_{PA}$ remain. The characteristic

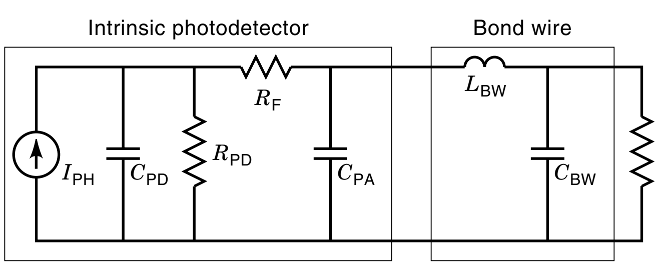

Figure 16. MSM photodetector equivalent circuit.

Table 4. Typical Values of the Elements to Be Introduced in the Equivalent Circuit

Element	Typical Value
C_{PD}	10–500 fF (see Fig. 15)
R_{PD}	$10^7 - 10^9$ Ω
R_F	1–100 Ω (41, 60, 61)
C_{PA}	10–100 fF (60, 61) ($<C_{PD}$)
L_{BW}	some tens of pH
C_{BW}	some fF

time constant corresponding to the photodetector impedance is then the well-known RC time constant.

For example, the RC time constant of a ($D = S = 1$ μm) MSM photodetector with a 50×50 μm^2 active area, loaded on 50 Ω resistance, is 4 ps, leading to an RC cut-off frequency as high as 40 GHz. On the other hand, assuming a saturation velocity of 5×10^6 cm/s, the corresponding transit time delay is 20 ps. All these values explain that the RC time constant is often not the dominant limiting factor of the MSM photodetectors' dynamic behavior. This is the reason we will now consider the carrier transit phenomenon.

Starting from the electric field distribution and the carrier paths described in Figs. 6 and 8, the transit time delay depends first on the interelectrode spacing, the absorbing layer thickness, and the bias voltage. It increases with the spacing and the absorbing layer thickness. On the other hand, in the regions where the carriers are photogenerated, the electric field must be sufficiently high to induce a saturation drift velocity for electrons and holes. Assuming at first that the absorbing layer (thickness W_a) is fully depleted, theoretical studies (62) predict that for a given finger spacing, the transit-time limited cut-off frequency is the highest when

$$\frac{S}{W_a} \approx 0.5$$

An example of such a characteristic is given in Fig. 17, which presents the cut-off frequency of GaInAs/AlInAs MSM photo-

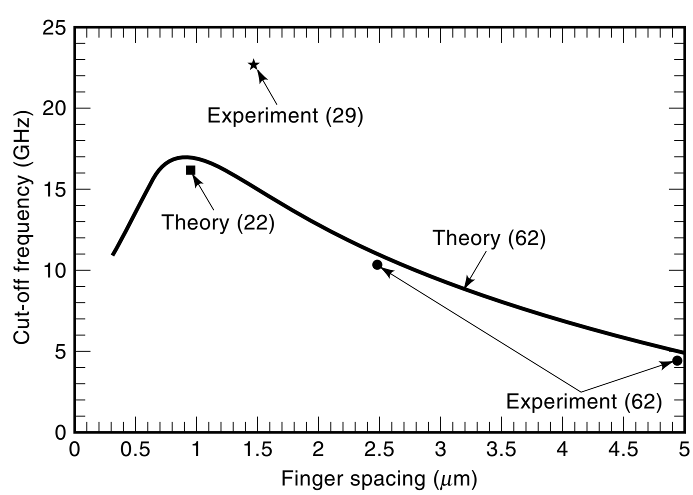

Figure 17. Cut-off frequency versus finger spacing for GaInAs/AlInAs MSM photodetector. The straight line represents theoretical result after (62), $W_a = 2$ μ, 500 Å AlInAs; the dots represent the experimental results after (62), $W_a = 2$ μm, 500 Å AlInAs; the square represents the theoretical result after (22), $W_a = 2$ μm, 500 Å AlInAs; and the star represents the experimental result after (29), $W_a = 1.5$ μm, 700 Å AlInAs, graded superlattice.

detectors versus finger spacing. We have joined theoretical (8,22,62) and experimental (29,62) results. The comparison between these results is difficult to carry out because generally experiments are performed with relatively high optical power (some milliwatts). This induces high carrier densities in the absorbing layer and as consequence an electric field screening (63) that modifies the carrier velocity distribution and thus increases the transit time delay. This phenomenon also occurs for high-input modulated light power (64) and depends strongly on the optical spot width. The specific electric field distribution due to the planar structure makes the MSM photodetector particularly sensitive to this factor. Moreover, for experiments under pulse operation, the cut-off frequency is derived from Fourier transform of the time response, which introduces additional errors. These reasons explain the differences between the results even if the overall behavior is the same.

Obviously, for thinner absorption layers, the obtained transit-time limited cut-off frequency is higher (22), particularly in the submicronic electrode spacing domain. More generally, in case of low penetration depth, because the majority of electron-hole pairs are photogenerated near the semiconductor surface (for III-V materials, the penetration depth is around 1 μm near cut-off wavelength) a semi-infinite absorption layer allows short transit time leading to very high cut-off frequencies. For example, a bandwidth of 105 GHz has been obtained on an MSM photodetector made by aluminum deposition on bulk GaAs with 0.5 μm electrode spacing (65); 300 GHz has been recorded by Chou et al. (5) on bulk GaAs with 0.1 μm electrode spacing by using high-resolution electron beam lithography. But for this electrode spacing domain, Monte Carlo simulations predict that the electron and hole pulse currents are separated because of the lower saturation drift velocity of holes. Moreover, the influence of parasitic elements becomes predominant, modifying the shape and the width of the output pulse (66). In the extreme case, for electrode spacing lower than the mean free path, the electronic transport is nonstationary and the transit time strongly decreases due to the electron velocity overshoot. This phenomenon permits reaching the terahertz frequency domain.

Anyway, the decrease of the absorbing layer thickness permits to reduction of the transit time. For example, Chou et al. (67) introduced an insulating AlGaAs-GaAs superlattice between the semi-insulating GaAs substrate and the 0.4 μm thick absorption layer in order to avoid the collection of carriers photogenerated in the substrate. In silicon, around 0.8 μm wavelength, a cut-off frequency higher than 100 GHz cannot be obtained because of the very low absorption coefficient. Particularly, the carriers photogenerated below the depletion region, which are collected after a long diffusion process toward the depleted zone, introduce a long tail to the photodetector pulse response. All these problems can be overcome by a local etching of the wafer back so as to get a very thin absorbing layer (52), or by using a specific insulating wafer, such as SIMOX (35) or sapphire (34). Obviously, these solutions lead to bandwidth increase at the expense of responsivity. If this latter is not of prime importance, it is possible to use an absorbing material with a very short carrier lifetime. The cut-off frequency is then limited by the recombination time and not by the carrier transit time. With this objective, low-temperature GaAs. Cr-doped GaAs, Fe-doped InGaAs, and amorphous silicon have been employed. The responsivity of such MSM photodiodes is lower than that obtained on pure bulk materials, but the bandwidth is enhanced. For these recombination time-limited MSM photodetectors, a submicronic electrode spacing is not required. All the above considerations concern very high-speed MSM photodetectors. Let us now consider the photodetectors were a high responsivity, as well as a bandwidth of a few tens of gigaherz, is needed.

Especially in the (1.3 μm to 1.55 μm) wavelength domain, where the absorption layer bandgap is small, the heterointerface between the enhancement barrier layer and the absorbing layer leads to carrier pileup, increasing the transit time. The carrier pileup also influences the photodetector photocurrent-voltage characteristic because of the recombinations that occur if the heterointerface electric field is not high enough for carriers to pass through (Fig. 13). As demonstrated theoretically and experimentally (23,68), the introduction of a transition layer smoothing the conduction and valence band discontinuities allows us to avoid this problem. As a typical example, the fall time of the pulse response measured on a GaInAs/AlInAs MSM photodetector (D = 2.5 μm, S = 2.5 μm, A = 30 × 30 μm^2, W_a = 0.8 μm) decreases from 19.3 ps to 15.7 ps by introducing a graded superlattice GaInAs-AlInAs (23). This results in a bandwidth enhancement from 18.1 GHz to 22.3 GHz (more than 20%).

Figure 18 presents the frequency and time responses with opaque and transparent fingers for a top-illuminated GaInAs-AlInAs MSM photodiode (D = 3 μm, S = 3 μm, A = 50 × 50 μm^2, W_a = 1 μm) grown on InP : Fe substrate (42). In this case, the carriers photogenerated under the electrodes lead to increasing the responsivity from 0.3 to 0.6 A/W (without antireflection coating) but also to reducing the bandwidth from 13 GHz to 6 GHz. In case of back illumination, the bandwidth reduction will be of the same order of magnitude (obviously, whatever the transparency of the electrodes is).

In order to review the various typical characteristics of the MSM photodetectors, we have gathered in Table 5 typical reported structures with their measured responsivity and cut-off frequency. We included silicon, GaAs, and InP based devices, with transparent or opaque fingers, top or back illuminated. Most of these photodetectors are transit-time limited and the one on low-temperature GaAs is recombination-time

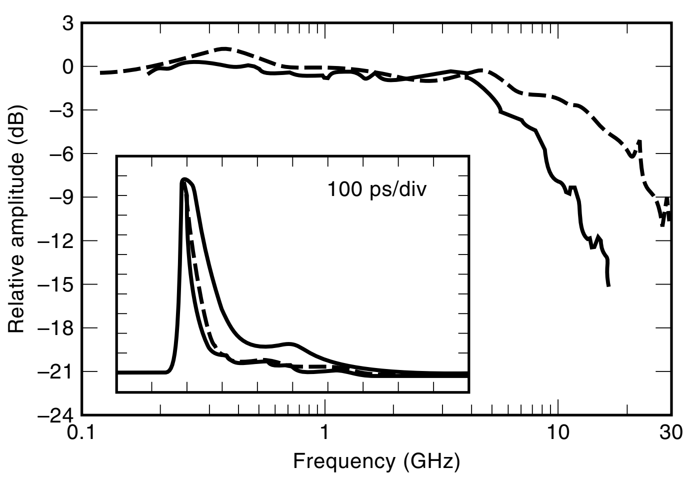

Figure 18. Frequency responses of MSM photodetectors with opaque Ti-Au fingers (dashed line) and transparent ITO(N2/H2) (dashed line) fingers. The active area is 2500 μm^2, the finger width and spacing are 3 μm, and the wavelength is 1.3 μm. This curve is reprinted from Seo et al., Ref. 42 with permission. ©1993 IEEE.

Table 5. Typical MSM Photodetector Material Structures with the Corresponding Measured Responsivity and Cut-off Frequency. The Noted Wavelength Is That of the Dynamic Measurement System. Some Structures of This Table Are also in Table 2 with Their Dark Current.

Ref.	Wavelength (μm)	Epitaxial Structure	Active Area (μm^2)	$D \times S$ (μm^2)	W_a (μm)	$\Re$ (A/W)	Cut-off Frequency
(5)	0.633	crist-Si substrate (P type)	10 × 10	0.1 × 0.1	semi-inf.	0.4	41 GHz
(35)	0.78	crist.-Si/SiO_2/Si (SIMOX wafer)	5 × 5	0.1 × 0.1	0.1	0.0057	140 GHz
(5)	0.633	GaAs(S.I.) substrate	10 × 10	0.1 × 0.1	semi-inf.	0.2	300 GHz
(5)	0.633	GaAs(S.I.)/LT-GaAs (1 μm)	10 × 10	0.3 × 0.3	semi-inf.	0.1	510 GHz
(18)	0.82	GaAs(S.I.)/GaAs/AlGaAs	75 × 75	2 × 4	semi-inf.	0.32	3.5 GHz
(22)	1.55	InP(S.I.)/GaInAs/AlInAs	50 × 50	1 × 1	1	0.35	17 GHz
(39)	1.3	InP(S.I.)/InP/GaInAs/InP	50 × 50	2 × 2	1	0.73	10 GHz
(41)	1.3	InP(Fe)/GaInAs(Fe)/InP(Fe)	100 × 100	1.5 × 1.5	2.5	0.35	4.8 GHz
(25)	1.54	InP(Fe)/InP/GaInAs/InP/GaInP	100 × 100	3 × 3	1	0.7**	2 GHz
(23)	1.3	InP(S.I.)/AlInAs/GSL/GaInAs/ GSL/AlInAs	30 × 30	2.5 × 1.5	0.8	0.36	20 GHz
(42)	1.3	InP(Fe)/AlInAs/GaInAs/ In(GaAl)As/AlInAs	50 × 50	3 × 3	1	0.8**	10 GHz
(28)	1.3	InP(S.I.)/AlInAs/GaInAs/ In(GaAl)As/AlInAs	17700	1 × 2	1	0.85*	4 GHz

*Back illumination; **Transparent fingers; GSL: graded superlattice; S.I.: semi-insulating

limited. This table gives also an idea of the trade-off between responsivity and cut-off frequency existing for this type of photodetector. In the (1.3 μm to 1.55 μm) wavelength domain, this trade-off leads to a low responsivity for bandwidths exceeding 20 GHz. For example, numerical modelling results show a responsivity lower than 0.15 A/W for a cut-off frequency higher than 45 GHz in the case of a InP/GaInAs/AlInAs photodetector with 0.3 μm electrode spacing (62). In fact, as for *pin* photodetectors, this trade-off can be overcome by using side-illuminated structures grown on an optical waveguide. Indeed, the absorbing layer grown on top of the waveguide can be very thin without giving the internal quantum efficiency up since the guided light is then progressively absorbed during its propagation. This is the main advantage of this type of structure.

Noise

Like all other semiconductor photodetectors, the MSM photodetector noise is related to different sources:

1. Thermal noise
2. $1/f^{\alpha}$ noise
3. Shot noise

Thermal noise intensity is theoretically frequency independent (white noise) and depends on the resistances existing in the whole equivalent circuit. In fact, the load resistance is generally the main part of the resistance that has to be taken into account, but finger resistance could have an influence, especially in the case of small finger width or if the electrode material has a relatively high resistivity. The thermal noise spectral density is given by

$$\langle I_{\mathrm{TH}^2} \rangle = 4kT/R \qquad (\text{in A}^2/\text{Hz}) \tag{18}$$

where T is the temperature and R the resistance of interest.

The $1/f^{\alpha}$ noise has a complex origin. Its spectral distribution is in $1/f^{\alpha}$ where α is close to 1, which makes it important for low frequencies. It has been notably related to material defects inducing various local lifetimes, these defects being localized at the semiconductor surface or interfaces. It is often higher in devices with horizontal current flow (such as MESFET e.g.) rather than in devices with vertical current flow. As for the shot noise, it is related to the randomness of photogeneration and transport processes. Its spectral density is given by

$$\langle I_{\mathrm{SH}^2} \rangle = 2q(I_{\mathrm{d}} + I_{\mathrm{PH}}) \quad (\text{in A}^2/\text{Hz}) \tag{19}$$

where I_d and I_{PH} are, respectively, the dark and photocurrent. Its spectral distribution is flat (white noise) up to the photodetector cut-off frequency, where it behaves like the photocurrent (69).

Consequently, the MSM photodetector noise depends, for a given device, on the frequency, the bias voltage, and obviously, the dark and photocurrents.

Assuming an illuminated photodiode with small dark current (some tens of nanoamperes) at the optimal bias voltage, the $1/f$ noise has been reported to be higher than the shot noise only for frequencies lower than 1 MHz or even lower (70). For higher frequencies, the shot noise is dominant and can be considered the main noise source of this type of photodetector (70,71). The reduction of this noise current leads thus to better sensitivity receivers. For high bias voltage, the shot noise is strongly enhanced if a gain phenomenon occurs. We know, as encountered for avalanche photodiodes, that the noise factor F_N depends particularly on the nature and on the distribution of the gain phenomenon in the material. Assuming that $I_{PH} \gg I_d$, the noise density is given by

$$\langle I_{\mathrm{SH}^2} \rangle = 2qI_{\mathrm{PH0}}G^2F_{\mathrm{N}} = 2qI_{\mathrm{PH0}}G^{2+x} \tag{20}$$

where I_{PH0} is the primary photocurrent (without gain), and G the gain. The different reported measurements demonstrate values of x much higher than those observed in the InP/GaInAs avalanche photodiodes ($x \le 1$). For example, Vinchant et al. (53) measured $x = 2.4$ and Wada et al. (71), $x = 1.6$. Moreover, close to breakdown, especially in GaInAs-based devices with an enhancement barrier layer, the $1/f$ noise increases with the internal electric field strength, exceeding the shot noise at higher frequencies. This behavior related to traps at the heterointerfaces makes the $1/f$ noise significant at frequencies in order of 100 MHz (22).

These results explain that the noise behavior of the MSM photodetector under optimum bias voltage is similar to those of the *pin* photodiode; moreover, the use of MSM photodetectors near breakdown is not of interest.

Scaling Rules

In spite of the great number of parameters influencing the MSM photodetector behavior, we will give some simple rules necessary to design such a structure. The responsivity being related to the absorbing layer thickness and the shadowing effect [Eq. (14)], the major problem is the bandwidth. Indeed, the transit phenomenon, generally simulated by using complicated bidimensional models (48,62,63), is difficult to predict realistically with simple calculations. However, it is possible to give a simple formula in order to have an idea of the structure suitable to a given application. In this way, the photodetector transfer function can be written

$$H(\omega) = \frac{1}{(1 + j\omega R_L C_{\mathrm{MSM}})} \frac{1}{(1 + j\omega\tau)} \tag{21}$$

where the first term introduces the RC time constant, C_{MSM} being calculated with Eq. (16), and the second term represents the transit influence. The transit-time delay is then given by (72)

$$\tau = \frac{S}{2v_{\mathrm{sat}}}\delta \tag{22}$$

where v_{sat} is the carrier saturation velocity (the same for electrons and holes) and δ a number generally between 1 and 2, which introduces a correction due to the curved nature of the field lines (see Fig. 8). Under these assumptions, the cut-off frequency is

$$f_c = \frac{1}{2\pi\sqrt{(R_L C_{\mathrm{MSM}})^2 + \tau^2}} \tag{23}$$

For example, Fig. 19 presents the cut-off frequency versus the photodiode area and the period in different cases: $S = W$ and

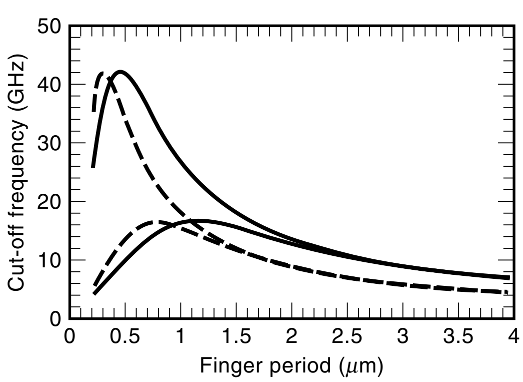

Figure 19. MSM photodetector cut-off frequency versus finger period for various surfaces and ratios S/W. The higher curves correspond to a 20×20 μm^2 surface while the lower ones to 50×50 μm^2. For all curves, we have taken: $\delta = 1.4$. Straight lines: $S = D$, dashed lines: $S = 3D$ and the load is 50 Ω.

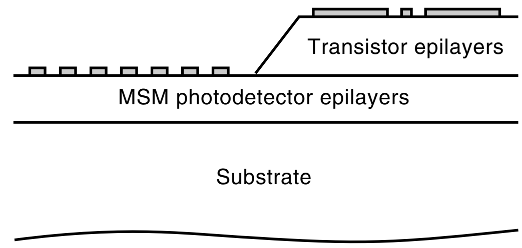

Figure 20. Integration scheme of MSM detector and transistors. The ohmic contacts of transistors are more often made before the common Schottky contact of MSM and FET's gate so as not to destroy these during the high temperature anneal of ohmic contacts.

$S = 3D$, for $R_L = 50$ Ω. The shape of each curve is due to the influence of capacitance and transit, the RC time delay being dominant for small periods (and small interelectrode spacing) and the transit-time delay becoming dominant for large periods. Obviously a trade-off leads to a maximum cut-off frequency, which increases strongly when decreasing area. Furthermore, a comparison of the cases $S = D$ and $S = 3D$ demonstrates that for a given period, the decrease of the finger width can be interesting since the resulting reduction of the shadowing effect is not at the expense of the bandwidth. Obviously, this result is acceptable as long as the finger resistance is not too high.

INTEGRATION

As can be seen in the above descriptions, several aspects make the MSM photodetector a favored candidate for the fabrication of high bandwidth monolithic integrated circuits. These are:

1. Planar configuration of electrodes
2. Use of undoped layers
3. Low capacitance
4. Low dark current

All these points make this photodiode particularly suitable for integration in a microwave strip or coplanar line. Indeed, this integration is needed for high-speed operation in order to reduce parasitics due to interconnections. On this topic, coplanar designs have been reported, such as those of Nakajima et al. (9), proposing a photodetector in a coplanar line directly integrated in a coaxial cable, or those of Kim et al. (28). In the first example, the photodetector is in the middle of the microwave line and it is connected by two accesses in quadripole configuration. On the contrary, in the second example, the photodiode has one electrode to the ground and needs only one microwave connector. It can be tested by using microwave measurement probes. The first configuration is used especially in cases of optical sampling [see, e.g., the optoelectronic AND gate and the inhibitor fabricated by Sugeta et al. (12)].

Optoelectronic integrated circuits (OEIC) combining both optoelectronic and electronic functions always constitute attractive technical and commercial subjects since they allow simultaneously the increase in performance of components by the decrease of parasitics and the decrease of manufacturing costs by reducing the handling and assembling of separate devices. The counterpart of this is sometimes and more often

Table 6. Advances in OEICs Associating MSM Detector and FETs. The Upper Part of the List Is Dedicated to 0.8 μm Wavelength Devices, the Lower One to 1.3 μm and 155 μm.

Ref.	MSM Characteristics: Active Area, $D \times S$ (μm)	Transistor (Type, Gate Length, Amp. Type)	Bandwidth	MSM Responsivity (A/W)	IC Responsivity (V/W)
(74)	100 × 100, 3, 3	MESFET, 2 μm, TZ	2 Gbits/s	0.2	400
(75)	75 × 75, 1, 3.25	MESFET, 1 μm, TZ diff. pair	3.2 GHz	0.45	
(76)	10 × 10, 1, 1	MESFET, 0.35 μm, TZ	5.2 GHz	0.2	60
(77)	25 × 25, 1, 1.5	c-HEMT, 0.3 μm, TZ	14 GHz	0.25	170
(78)	InP, 1.5, 2.5	FET, 1.1 μm	200 Mbits/s	0.9	
(79)	30 × 30, InAlAs, 1,1	InGaAs HEMT, 1 μm (GaAs subst.)		0.45	
(20)	25 × 25, GaAs, 0.75, 1	GaAs HEMT, 0.3 μm, TZ (GaAs subst.)	430 MHz	0.08	2100
(80)	50 × 50, InP, 0.5, 0.5	InGaAs HEMT, 0.3 μm to 1 μm	16 GHz	0.26	

a larger complexity in technological process. The four previously mentioned characteristics of the MSM photodetector are significant assets compared to its main competitor for integration objectives, the *pin* photodiode. Nevertheless, the *pin* advances a better responsivity, which is not a trivial detail. But from a technological point of view, the integration scheme proves easy: the MSM detector is built on the buffer layer (or even more simply on the substrate) and transistor—mainly field effect transistors (FET)—epilayers are grown above (Fig. 20). This often leads to a very weak difference in height between MSM and transistor planes, which facilitates the interconnections. Moreover, since transistor gate and MSM finger metallization is often the same, they are usually deposited simultaneously, thus reducing the number of technological steps.

Owing to a very simple manufacturing process on GaAs material system and a total compatibility with FET technology, the first integrated photoreceivers combining MSM and metal-semiconductor field effect transistors (MESFET) have been produced in this material system. After the first attempt—association with a high-impedance (HZ)–type amplifier (73)—which mainly demonstrated the feasibility of such integration, all subsequent ICs used a transimpedance (TZ) design. The MSM detector is made either on the substrate or on the buffer layer, which, in any case, is needed for the transistor fabrication. Various forms of FETs can be used, namely more frequently MESFET or high electron mobility transistor (HEMT), different ICs are listed in Table 6 (upper part). More recent devices exhibit a bandwidth greater than 10 GHz and very good performance. Unfortunately, the 0.8 μm wavelength is not in favor with optical communications either in long-haul (high bit rate) systems or even in short-haul (distribution) ones. It is then preferable to move to longer wavelengths: 1.3 μm and 1.55 μm. Use of GaInAs(P)/InP MSM detectors is then required. For these materials (see section on material systems), MSM loses its technological simplicity since a much more complicated epitaxy is needed. Different enhancement layers can be used, which lead to many integrable devices. Different kinds of transistors can also be made, either in the InP or GaAs material system. Depending on the available device technology, expertise of heteroepitaxy, and knowledge of the research teams involved, several attempts (some of them are listed in the above table) tend to demonstrate that integrated photoreceivers can be made mixing various transistor and MSM types. In all cases, the frequency response of the long-wavelength MSM detector (see Section on dynamic behavior) governs the response of the integrated photoreceiver.

Because of the very large range of possible design rules and the related trade-offs between the performance of the optoelectronic (the MSM detector) and electronic (the transistors) components, no real conception scheme has emerged up to now, and so no integrated photoreceiver of this type is currently commercially available.

BIBLIOGRAPHY

1. S. M. Sze, *Physics of Semiconductor Devices,* 2nd ed., New York: Wiley, 1981.
2. S. M. Sze, D. J. Coleman Jr., and A. Loya, *Current transport in Metal-Semiconductor-Metal structure,* Solid State Electronics, New York: Pergamon Press, 1971, vol 14, pp 1209–1218.
3. J. B. D. Soole et al., High speed performance of OMCVD grown InAlAs/InGaAs MSM photodetectors at 1.5 μm and 1.3 μm wavelengths, *IEEE Photon. Tech. Lett.* **1**: 250–252, 1989.
4. A. Aboudou et al., GaAlAs/GaAs planar photoconductors and MSM photodetectors monolithically integrated with HIGFETs: application for optical dock distribution, *IEE Proc. J* **139** (1): 83–87, 1992.
5. S. Y. Chou and M. Y. Liu, Nanoscale tera-hertz Metal-Semiconductor-Metal photodetectors, *IEEE J. Quantum Electr.,* **28**: 2358–2368, 1992.
6. M. Ito and O. Wada, Low dark current GaAs Metal-Semiconductor-Metal photodiodes using Wsi_x contacts. *IEEE J. Quantum Electr.,* **22**: 1073–1077, 1986.
7. L. Yang et al., High performance of Fe:InP/InGaAs Metal-Semiconductor-Metal photodetector grown by metalorganic vapor phase epitaxy. *IEEE Photon. Tech. Lett.* **2**: 56–58, 1990.
8. I. S. Ashour et al., Comparison between GaAs and AlInAs/GaInAs MSM PD for microwave and millimeter-wave applications using a two dimensional bipolar physical model. *Micr. Opt. Tech. Lett.* **9** (1): 52–57, 1995.
9. K. Nakajima et al., Properties and design theory of ultrafast GaAs Metal-Semiconductor-Metal photodetector with symmetrical Schottky contacts, *IEEE Trans. Electron Devices,* **37**: 31–35, 1990.
10. W. Wohlmuth et al., Engineering the Schottky barrier heights in InGaAs Metal-Semiconductor-Metal photodetectors, *Proc. SPIE,* **3006**: 52–60, 1997.
11. W. C. Koscielniak et al., Dark current characteristics of GaAs Metal-Semiconductor-Metal photodetectors, *IEEE Trans. Electron. Devices,* **37**: 1623–1629, 1990.
12. T. Sugeta et al., Metal-Semiconductor-Metal photodetector for high speed optoelectronic circuits. *Proc. 11th Conf. Solid State Devices Jpn. J. Appl. Phys.* **19** Suppl 19-1: 459–464, 1980.

13. H. H. Wehmann et al., Dark current analysis of InGaAs MSM photodetectors on Silicon substrate. *IEEE Trans. Electron Devices,* **43**: 1505–1509, 1996.
14. S. Kollakowski et al., Fully passivated AR coated InP/InGaAs MSM photodetectors, *IEEE Photon. Tech. Lett.* **6**: 1324–1326, 1994.
15. W. Wohlmuth, P. Fay, C. Caneau, and I. Abesida, Low dark current, long wavelength Metal-Semiconductor-Metal photodetectors, *Electron. Lett.* **32** (3): 249–250, 1996.
16. H. T. Griem et al., Long wavelength (1.0-1.6 μm) InAlAs/In(GaAl)As/InGaAs Metal-Semiconductor-Metal photodetector. *Appl. Phys. Lett.* **56** (11): 1067–1068, 1990.
17. J. H. Burroughes, H-Mesfet compatible GaAs/AlGaAs MSM photodetector, *IEEE Photon. Techn. Lett.* **3**: 660–662, 1991.
18. C. X. Shi et al., High performance undoped InP/N InGaAs MSM photodetectors grown by LP-MOVPE, *IEEE Trans. Electron Devices,* **39**: 1028–1031, 1992.
19. O. Vendier, N. M. Jokerst, and R. P. Leavitt, High efficiency thin-film GaAs MSM Photodetectors, *Electron. Lett.* **32** (4): 394–395, 1996.
20. V. Hurm et al., 1.3 μm monolithic integrated optoelectronic receiver using an InGaAs MSM photodiode and AlGaAs/GaAs HEMTs grown on GaAs, *Electron. Lett.* **31** (1): 67–68, 1995.
21. M. A. Matin et al., Very low dark current InGaP/GaAs MSM Photodetector using semi transparent and opaque contacts, *Electron. Lett.* **32** (8): 766–767, 1996.
22. J. B. D. Soole and H. Schumacher, InGaAs Metal-Semiconductor-Metal photodetectors for long wavelength optical communications. *IEEE J Quantum Electr.* **27**: 737–752, 1991.
23. Y. G. Zhang, A. Z. Li, and J. X. Chen, Improved performance of InAlAs-InGaAs-InP MSM photodetectors with graded superlattice structure grown by gas source MBE. *IEEE Photon. Tech. Lett.* **8**: 830–832, 1996.
24. H. Schumacher et al., An investigation of the optoelectronic response of GaAs/InGaAs MSM photodetectors. *IEEE Electr. Device Lett.* **9**: 607–609, 1988.
25. R. H. Yuang et al., High responsivity InGaAs MSM photodetectors with semi transparent Schottky contacts. *IEEE Photon. Tech. Lett.* **7**: 1333–1335, 1995.
26. W. P. Hong, G. K. Chang, and R. Bhat, High performance AlGaAs/InGaAs MSM photodetectors grown by OMCVD. *IEEE Trans. Electron. Devices* **36**: 659–662, 1989.
27. P. W. Leech et al., HgCdTe Metal-Semiconductor-Metal photodetectors, *IEEE Trans. Electron. Devices,* **40**: 1365–1370, 1993.
28. J. H. Kim et al., High performance back-illuminated InGaAs/InAlAs MSM photodetector with a record responsivity of 0.96A/W, *IEEE Photon. Tech. Lett.* **4**: 1241–1245, 1992.
29. O. Wada et al., Very high speed GaInAs Metal-Semiconductor-Metal photodiode incorporating an AlInAs/GaInAs graded superlattice, *Appl. Phys. Lett.* **54** (1): 16–17, 1989.
30. S. Tiwari et al., 1.3 μm GaSb Metal-Semiconductor-Metal photodetectors, *IEEE Photon. Tech. Lett.* **4**: 256–25, 1992.
31. S. V. Averin et al., Low dark current quasi-Schottky barrier MSM photodiodes structures on N-GaInAs with P+ GaInAs cap layer, *Electron. Lett.* **28** (11): 992–995, 1992.
32. A. Aboudou et al., Ultralow dark current GaAlAs/GaAs MSM photodetector, *Electron. Lett.* **27** (10): 793–794, 1991.
33. Y. G. Zhang, A. Z. Li, and A. G. Milnes, Metal-Semiconductor-Metal ultraviolet photodetectors using 6H-SiC, *IEEE Photon. Tech. Lett.* **9**: 363–364, 1997.
34. C. C. Wang et al., Comparison of the picosecond characteristics of silicon and silicon-on-sapphire Metal-Semiconductor-Metal photodiodes, *Appl. Phys. Lett.* **64** (26): 3578–3580, 1994.
35. M. Y. Liu, E. Chen, and S. Y. Chou, 140GHz Metal-Semiconductor-Metal photodetectors on silicon-on-insulator substrate with a scaled active layer, *Appl. Phys. Lett.* **65** (7): 887–888, 1994.
36. S. Y. Chou, Y. Liu, and T. F. Carruthers, 32GHz Metal-Semiconductor-Metal photodetectors on crystalline silicon, *Appl. Phys. Lett.* **61** (15): 1760–1762, 1992.
37. B. F. Levine et al., 1 Gb/s Si high quantum efficiency monolithically integrable λ = 0.88 μm detector, *Appl. Phys. Lett.* **66** (22): 2984–2986, 1995.
38. L. H. Laih et al., High performance Metal-Semiconductor-Metal photodetector with a thin hydrogenated amorphous silicon layer on crystalline silicon, *Electron. Lett.* **31** (24): 2123–2124, 1995.
39. M. A. Matin et al., High responsivity InGaAs/InP based MSM Photodector operating at 1.3 μm wavelength, *Microw. Opt. Technol. Lett.* **12** (6): 310–313, 1996.
40. K. Kajiyama, Y. Mizushima, and S. Sakata, Schottky barrier height of N-InGaAs diodes, *Appl. Phys. Lett,* **23** (8): 458–459, 1973.
41. E. H. Böttcher et al., Ultrafast semiinsulating InP : Fe-InGaAs : Fe-InP MSM photodetectors: Modeling and performance, *IEEE J. Quantum Electr.* **28**: 2343–2357, 1992.
42. J. W. Seo et al., Application of Indium-Tin-Oxide with improved transmittance at 1.3 μm for MSM photodetectors, *IEEE Photon. Tech. Lett.* **5**: 1313–1315, 1993.
43. A. Bartels et al., Performance of InGaAs Metal-Semiconductor-Metal photodetectors on Si, *IEEE Photon. Techn. Lett.* **8**: 670–672, 1996.
44. D. L. Rogers et al., High speed 1.3 μm GaInAs Detectors fabricated on GaAs substrates, *IEEE Electr. Device Lett.* **9**: 515–517, 1988.
45. D. A. Humphreys et al., Measurement of absorption coefficient of GaInAs over the wavelength range 1.0–1.7 μm, *Electron. Lett.* **21** (25): 1187–1189, 1985.
46. W. Gao et al., InGaAs Metal-Semiconductor-Metal photodiodes with transparents Cadmium Tin Oxide Schottky contacts, *Appl. Phys. Lett.* **65** (15): 1930–1932, 1994.
47. C. C. Chu et al., Performance enhancement using Wsix/ITO electrodes in InGaAs/InAlAs MSM photodetectors, *Electron. Lett.* **31** (19): 1692–1694, 1995.
48. E. Sano, Two-dimensional ensemble Monte Carlo calculation of pulse responses of submicrometer GaAs Metal-Semiconductor-Metal photodetectors, *IEEE Trans. Electron. Devices* **38**: 2075–2081, 1991.
49. J. J. Kuta et al., Polarization and wavelength dependence of Metal-Semiconductor-Metal photodetector response, *Appl. Phys. Lett.* **64** (2): 140–142, 1994.
50. E. Chen and S. Y. Chou, A wavelength detector using monolithically integrated subwavelength Metal-Semiconductor-Metal photodetectors, *Proc SPIE* **3006**: 61–67, 1997.
51. E. Chen and S. Y. Chou, High efficiency and high speed Metal-Semiconductor-Metal photo-detectors on Si-on-insulator substrates with buried backside reflectors, *Proc SPIE* **3006**: 74–82, 1997.
52. H. C. Lee and B. V. Zeghbroeck, A novel high speed silicon MSM photodetector operating at 830nm wavelength, *IEEE Electr. Device Lett.* **16**: 175–177, 1995.
53. J. F. Vinchant et al., Monolithic integration of a thin and short Metal-Semiconductor-Metal photodetector with a GaAlAs optical inverted rib waveguide on a GaAs semi insulating substrate, *Appl. Phys. Lett.* **55** (19): 1966–1968, 1989.
54. J. B. D. Soole et al., Waveguide integrated MSM photodetector on InP, *Electron. Lett.* **24** (24): 1478–1480, 1988.

55. L. Yang, A. S. Sudbo, and W. T. Tsang, GaInAs Metal-Semiconductor-Metal photodetectors with Fe : InP barrier layers grown by chemical beam epitaxy, *Electron. Lett.* **25** (22): 1479–1481, 1989.

56. J. H. Burroughes and M. Hargis, 1.3 μm InGaAs MSM photodetector with abrupt InGaAs/AlInAs interface, *IEEE Photon. Tech. Lett.* **3**: 532–534, 1991.

57. M. Klingenstein et al., Photocurrent gain mechanisms in Metal-Semiconductor-Metal photodetectors, *Solid State Electron* **37** (2): 333–340, 1994.

58. J. P. Vilcot, J. L. Vaterkowski, and D. Decoster, Temperature effects on high gain photoconductive detectors, *Electron. Lett.* **20** (2): 86–87, 1984.

59. Y. C. Lim and R. A. Moore, Properties of alternately charged coplanar parallel strips by conformal mapping, *IEEE Trans. Electron. Devices* **15**: 173–180, 1968.

60. W. C. Koscielnak, J. L. Pelouard, and M. A. Littlejohn, Intrinsic and extrinsic response of GaAs Metal-Semiconductor-Metal photodetector, *IEEE Photon. Tech. Lett.* **2**: 125–127, 1990.

61. J. W. Chen, D. K. Kim, and M. B. Das, Transit time limited high frequency response characteristics of MSM photodetectors. *IEEE Trans. Electron. Devices* **43**: 1839–1843, 1996.

62. I. S. Ashour et al., Cutoff frequency and responsivity limitation of AlInAs/GaInAs MSM PD using a two dimensional bipolar physical model, *IEEE Trans. Electron. Devices* **42**: 231–237, 1995.

63. C. Moglestue et al., Picosecond pulse response characteristics of GaAs Metal-Semiconductor-Metal photodetectors, *J Appl. Phys.* **70** (4): 2435–2448, 1991.

64. I. S. Ashour et al., High optical power nonlinear dynamic response of AlInAs/GaInAs MSM Photodiode, *IEEE Trans. Electron. Devices* **42**: 828–834, 1995.

65. B. J. Van Zeghbroeck et al., 105GHz bandwidth Metal-Semiconductor-Metal photodiode. *IEEE Electr. Device Lett.* **9**: 527–529, 1988.

66. W. C. Koscielnak, J. L. Pelouard, and M. A. Littlejohn, Dynamic behavior of photocarriers in a GaAs Metal-Semiconductor-Metal photodetector with sub-half-micron electrode pattern, *Appl. Phys. Lett.* **54** (6): 567–569, 1989.

67. S. Y. Chou, Y. Liu, and P. B. Fischer, Tera-hertz GaAs Metal-Semiconductor-Metal photodetectors with 25 nm finger spacing and width, *Appl. Phys. Lett.* **61** (4): 477–479, 1992.

68. E. Sano et al., Performance dependence of InGaAs MSM photodetectors on barrier enhancement layer structure, *Electron. Lett.* **28** (13): 1220–1221, 1992.

69. J. P. Gouy et al., Microwave noise performance and frequency response of PIN GaInAs photodiodes, *Microw. Opt. Technol. Lett.* **3** (2): 47–49, 1990.

70. H. Schumacher et al., Noise behavior of InAlAs/GaInAs MSM photodetectors, *Electron. Lett.* **26** (9): 612–613, 1990.

71. O. Wada et al., Noise characteristics of GaAs Metal-Semiconductor-Metal Photodiodes, *Electron. Lett.* **24** (25): 1574–1575, 1988.

72. J. Burm et al., Optimization of high speed Metal-Semiconductor-Metal photodetectors, *IEEE Photon. Tech. Lett.* **6**: 722–724, 1994.

73. M. Ito et al., Monolithic integration of a Metal-Semiconductor-Metal photodiode and a GaAs preamplifier, *IEEE Electr. Device Lett.* **5**: 531–532, 1984.

74. D. L. Rogers, Monolithic integration of a 3Ghz detector/preamplifier using a refractory gate ion implanted MESFET process, *IEEE Electr. Device Lett.* **7**: 600–601, 1986.

75. H. Hamaguchi et al., GaAs optoelectronic integrated receiver with high output fast response characteristics, *IEEE Electr. Device Lett.* **8**: 39–41, 1987.

76. C. S. Harder et al., 5.2 GHz bandwidth monolithic GaAs optoelectronic receiver, *IEEE Electr. Device Lett.* **9**: 171–173, 1988.

77. V. Hurm et al., 14 GHz bandwidth MSM photodiode AlGaAs/GaAs HEMT monolithic integrated optoelectronic receiver, *Electron. Lett.* **29** (1): 9–10, 1993.

78. L. Yang et al., Monolithically integrated InGaAs/InP MSM-FET photoreceiver prepared by chemical beam epitaxy, *IEEE Photon. Tech. Lett.* **2**: 59–61, 1990.

79. W. P. Hong et al., InAlAs/InGaAs MSM photodetectors and HEMT's grown by MOCVD on GaAs substrates, *IEEE Trans. Electron. Devices* **39**: 2817–2818, 1992.

80. M. Horstmann et al., 16Ghz bandwidth MSM photodetector and 45/85GHz ft/fmax HEMT prepared on an identical InGaAs/InP layer structure, *Electron. Lett.* **32** (8): 763–764, 1996.

J. A. Harari
J. P. Vilcot
D. J. Decoster
Institut d'Electronique et de Microélectronique du Nord